ISSN 1063-7834, Physics of the Solid State, 2025, Vol. 67, No. 10, pp. 918–931. © Pleiades Publishing, Ltd., 2025.

Unveiling the Properties of $FrBX_3$ (B = Pb, Zr; X = Br, Cl) Inorganic Metal Halide Perovskites: Electronic, Optical, and Mechanical Perspectives

I. Bensehil[a,b], H. Baaziz[c,d,*,], T. Ghellab[c,d], F. Djeghloul[b,e], S. Zaiou[b,f], and Z. Charifi[c,d]**

[a] *Faculty of Technology, University of M'sila, University Pole, Road Bordj Bou Arreridj, M'sila, 28000 Algeria*
[b] *Laboratory of Surfaces and Interfaces Studies of Solid Materials, Ferhat Abbas Setif 1 University, Setif, Algeria*
[c] *Department of Physics, Faculty of Science, University of M'sila, M'sila, 28000 Algeria*
[d] *Laboratory of Physics and Chemistry of Materials, University of M'sila, M'sila, Algeria*
[e] *Department of Basic Education in Technology, Ferhat Abbas Setif 1 University, Setif, 19000 Algeria*
[f] *Faculty of Natural and Life Sciences, Ferhat Abbas Setif 1 University, Setif, 19000 Algeria*
**e-mail: hakim.baaziz@univ-msila.dz*
***e-mail: baaziz_hakim@yahoo.fr*

Received June 2, 2025; revised August 3, 2025; accepted August 10, 2025

Abstract—This study provides a comprehensive investigation into the structural, optoelectronic, and elastic properties of inorganic metal halide perovskites $FrBX_3$ (B = Pb, Zr; X = Br, Cl) using first-principles calculations based on density functional theory (DFT). Structural analysis confirms the stability of these perovskite phases through optimized lattice parameters and positive formation energies. Electronic band structure calculations reveal that $FrZnX_3$ compounds exhibit direct band gaps, while $FrPbX_3$ compounds possess indirect band gaps. Using the GGA-PBE functional, the band gaps are found to decrease in the order: $FrPbCl_3$ (2.237 eV), $FrPbBr_3$ (1.795 eV), $FrZnCl_3$ (1.185 eV), and $FrZnBr_3$ (0.057 eV), highlighting their potential for photovoltaic applications, particularly in solar energy harvesting. The optical properties, evaluated via dielectric functions, absorption coefficients, and refractive indices, demonstrate strong absorption in the visible region, suggesting their suitability as efficient light-absorbing materials. Furthermore, the elastic properties, including elastic constants, bulk modulus, shear modulus, and Poisson's ratio, confirm the mechanical stability and ductility of all studied compounds, as they satisfy the Born stability criteria. Moreover, the calculated elastic anisotropy indicates that these materials exhibit moderate directional dependence in their mechanical response, which is advantageous for thin-film fabrication processes. Overall, the combination of favorable electronic, optical, and mechanical properties makes these Fr-based perovskites promising candidates for use in next-generation photovoltaic devices and other optoelectronic applications.

Keywords: inorganic metal halide perovskites, electronic and optical properties, mechanical stability
DOI: 10.1134/S106378342560219X

1. INTRODUCTION

Halide perovskites (HPs), usually expressed by the general formula ABX_3, where A stands for a monovalent cation (such as methylammonium (MA^+), formamidinium (FA^+), or cesium (Cs^+)), B for a divalent metal cation (lead (Pb^{2+}) or tin (Sn^{2+})), and X for a halide anion (chloride (Cl^-), bromide (Br^-), or iodide (I^-)) have emerged as a versatile and highly promising class of materials due to their exceptional optoelectronic properties [1–4]. These materials have revolutionized the field of photovoltaics, achieving remarkable progress in solar cell efficiency due to their intrinsic properties, such as high absorption coefficients [5], tunable bandgaps, long carrier diffusion lengths, and low exciton binding energies. Beyond their application in photovoltaics, HPs exhibit a range of multifunctional properties, including strong photocatalytic activity [6], exceptional photovoltaic performance [7], piezoelectricity [8], and ferroelectricity [9]. These characteristics have catalyzed extensive research into their potential applications across various fields such as light-emitting diodes (LEDs) [10], lasers [11], field-effect transistors (FETs) [12], and photodetectors [13]. Despite impressive advancements, particularly in achieving power conversion efficiencies (PCE) of 25.7% in solar cells and LED efficiencies up to 23.4% [14], halide perovskite technologies continue to confront critical challenges. Key areas requiring further improvement include long-term stability of devices under operational and environmental stress, reducing the toxicity linked to lead-based compounds, and

enhancing overall device efficiency through targeted compositional and structural engineering strategies.

Recent research into perovskite materials have focused on compositional engineering, particularly through cation substitution at the A and B sites, to tailor electronic and optical properties. For instance, substituting alkali metals such as Li, Na, K, Rb, and Cs at the A site has demonstrated considerable improvements in photovoltaic performance [15]. Studies, such as those by Wittig et al. [15], have underscored the tunability of band gaps in $CsPbX_3$-based materials, offering a pathway to engineer materials with desirable absorption characteristics across the visible spectrum. Similarly, Pitriana et al. [16] reported that $APbI_3$ perovskites (A = Li, Na, K, Rb, Cs) exhibit semiconducting behavior well-suited for solar cell absorbers, emphasizing the versatility of alkali cation incorporation in optimizing optoelectronic performance.

Although numerous studies have been conducted on A-site cation substitutions in halide perovskites, francium has received little attention. This is mainly due to its high radioactivity, short half-life, and rare natural abundance, all of which pose significant experimental and safety challenges. Nonetheless, understanding the influence of heavy, radioactive elements on the structural and electronic properties of perovskites presents a unique opportunity to broaden their potential applications. Hasana et al. [10] have demonstrated that Fr-based perovskites, specifically $FrBX_3$ (B = Ge, Sn; X = Cl, Br, I), possess strong optical conductivity, minimal reflectivity, and high absorption coefficients, positioning them as viable candidates for photovoltaic and optoelectronic devices. Notably, $FrGeI_3$ was identified as a leading material for such applications due to its favorable electronic and mechanical properties. Moreover, the inherent radioactivity of Fr-based perovskites opens up intriguing possibilities for specialized applications, particularly in fields such as nuclear medicine and advanced imaging technologies.

Lead-free perovskites have garnered attention as alternatives to mitigate toxicity concerns associated with lead-containing compounds. Bushra et al. [17] investigated $FrBCl_3$ (B = Zn, Cd) perovskites, revealing their indirect band gaps, robust optical absorption, and mechanical stability. These findings highlight the potential of Fr-based perovskites in thin-film technologies, where mechanical flexibility and ductility are essential. Furthermore, their high Debye temperatures indicate favorable thermal stability, a critical factor for device longevity.

The unique combination of tunable electronic band structures, strong optical absorption, and mechanical stability in $FrBX_3$ perovskites (B = Pb, Zr; X = Br, Cl) opens a broad spectrum of applications. One of the most prominent applications is in photovoltaic devices. These materials, with suitable band gaps and high absorption coefficients, are promising candidates for solar cell absorbers. Their ability to harvest sunlight efficiently can lead to the development of next-generation photovoltaic technologies with enhanced power conversion efficiencies. In addition to photovoltaics, $FrBX_3$ perovskites exhibit exceptional potential for optoelectronic applications. Their strong optical conductivity and low reflectivity make them ideal for use in devices such as light-emitting diodes (LEDs), photodetectors, and lasers. These properties enable the fabrication of devices with improved luminous efficiency, fast response times, and broad spectral sensitivity, which are crucial for high-performance optoelectronic systems.

In this work, we examine how the structural, electrical, optical, and mechanical properties of Fr-based halide perovskites with the general formula $FrBX_3$ (B = Pb, Zr; X = Br, Cl) are affected by B-site cation substitution. By incorporating francium at the A site and varying the B-site cation between lead (Pb) and zirconium (Zr), we investigate how differences in ionic radius and atomic mass impact the overall behavior of these materials. The contrasting electronic configurations and chemical characteristics of Pb and Zr offer a unique opportunity to study the interplay between lattice distortions, band structure modifications, optical absorption, and mechanical stability. First-principles calculations within the density functional theory (DFT) framework are employed to comprehensively characterize these compounds, uncover the fundamental mechanisms governing their properties, and evaluate their potential for use in photovoltaics, optoelectronics, radiation detection, and thin-film technologies.

2. COMPUTATIONAL METHODS

The structural, electronic, optical, and mechanical properties of the $FrBX_3$ (B = Pb, Zr; X = Br, Cl) inorganic metal halide perovskites were investigated using first-principles calculations within the framework of density functional theory (DFT), as implemented in the CASTEP code [18]. The exchange-correlation energy was treated using the generalized gradient approximation (GGA) with the Perdew–Burke–Ernzerhof (PBE) functional, which is widely used due to its reasonable accuracy in predicting structural and electronic properties. To effectively model the interactions between ions and valence electrons, Vanderbilt-type ultrasoft pseudopotentials [19] were employed, enabling accurate calculations at a reduced plane-wave cutoff energy.

Geometry optimizations were performed using the Broyden–Fletcher–Goldfarb–Shanno (BFGS) algorithm until the following convergence thresholds were met: total energy within 5×10^{-6} eV/atom, maximum force less than 0.01 eV/Å, maximum atomic displacement less than 5×10^{-4} Å, and stress within 0.02 GPa.

These criteria ensured well-relaxed structures suitable for subsequent property calculations. The Brillouin zone was sampled using the Monkhorst–Pack scheme with a k-point grid of 12 × 12 × 12 for structural optimization. For electronic structure and density of states (DOS) calculations, a denser k-point mesh of 30 × 30 × 30 was used to capture finer details of the band structure. The plane-wave basis set cutoff energy was fixed at 600 eV after performing convergence tests to ensure reliable and accurate results without unnecessary computational cost.

The mechanical properties, essential for evaluating material stability and suitability for device fabrication, were determined by calculating the second-order elastic constants (C_{ij}) via the finite strain approach [20]. Small deformations were applied to the equilibrium structures, and the resulting stress tensors were analyzed to extract the elastic constants. From the C_{ij} values, key mechanical parameters, including the bulk modulus (B), shear modulus (G), and Young's modulus (E), were computed using the Voigt, Reuss, and Hill averaging schemes [21–23], offering a comprehensive understanding of the materials' resistance to deformation. Additionally, the Poisson's ratio (ν) and Pugh's ratio (B/G) were derived to assess ductility and mechanical stability, which are critical for practical applications.

Optical properties were computed based on the frequency-dependent dielectric function, calculated using the linear response formalism within CASTEP. A k-point mesh of 20 × 20 × 20 was adopted to ensure adequate resolution of optical transitions. From the complex dielectric function, various optical constants—such as the refractive index, absorption coefficient, reflectivity, and energy loss function—were derived using established theoretical relations [24]. These parameters are essential for assessing the potential of $FrBX_3$ perovskites in optoelectronic applications, including solar cells and photodetectors, where strong light absorption and favorable optical behavior are desired.

This computational framework provides a systematic approach to exploring the effects of substituting different B-site cations (Pb and Zr) and halogen anions (Br and Cl) on the physical properties of Fr-based perovskites, offering valuable insights into their potential for advanced technological applications.

3. RESULTS AND DISCUSSION

3.1. Structural Aspects

The structural properties of $FrBX_3$ (B = Pb, Zn; X = Br, Cl) perovskite compounds were investigated in the cubic Pm-3m space group (no. 221) within the non-magnetic phase. This crystal structure adopts a typical perovskite configuration, characterized by a three-dimensional network of corner-sharing BX_6 octahedra. In this arrangement, the larger Fr cations occupy the cubic voids formed by the octahedral framework, providing structural stability and ensuring overall charge balance.

In the optimized unit cell, Fr atoms are positioned at the Wyckoff site (0, 0, 0), B-site cations (Pb or Zn) are located at the body center (0.5, 0.5, 0.5), and halogen atoms (Br or Cl) occupy the face-centered positions at (0.5, 0, 0.5), (0.5, 0.5, 0), and (0, 0.5, 0.5). This configuration results in each B-site cation being octahedrally coordinated by six halogen atoms, forming nearly perfect BX_6 octahedra due to the inherent cubic symmetry. The Fr cations, located at the cube corners, are coordinated by twelve halogen atoms, emphasizing the strong ionic interactions that stabilize the structure.

To determine the equilibrium structural parameters, total energy versus unit cell volume calculations were performed using the Generalized Gradient Approximation (GGA) and fit to the Birch–Murnaghan equation of state [25]. The resulting energy–volume relationships are depicted in Fig. 1, while Table 1 presents the equilibrium lattice constants (a_0), volumes (V_0), bulk moduli (B_0), pressure derivatives (B'), ground-state energies (E_{coh}), and formation energies (ΔH_f).

The total energy versus volume curves in Fig. 1 exhibit the expected parabolic profiles, each reaching a minimum at its equilibrium volume, thereby con-

Table 1. Calculated equilibrium lattice constant (a_0 (Å)), volume (V_0 (Å^3)), bulk modulus (B (GPa), pressure derivative (B'), cohesive energy (E_{coh}), and formation energy (E_{for}) for $FrBX_3$ (where B = Pb, Zr and X = Br, Cl)

Alloys	a_0, Å	V_0, Å^3	B_0, GPa	B'	E_{coh}, eV	E_{for}, eV/atom
$FrZnCl_3$	5.111	133.420	32.97	4.70	–3469.43	–2.95
	5.10 [17]	132.76 [17]			3469.44 [17]	
$FrZnBr_3$	5.395	157.00	27.1364	5.03567	–3341.19	–2.59
$FrPbCl_3$	5.765	191.637	21.096	4.497	–3419.78	–3.49
$FrPbBr_3$	6.015	217.578	18.24	4.64	–3291.68	–3.16
	6.01458					

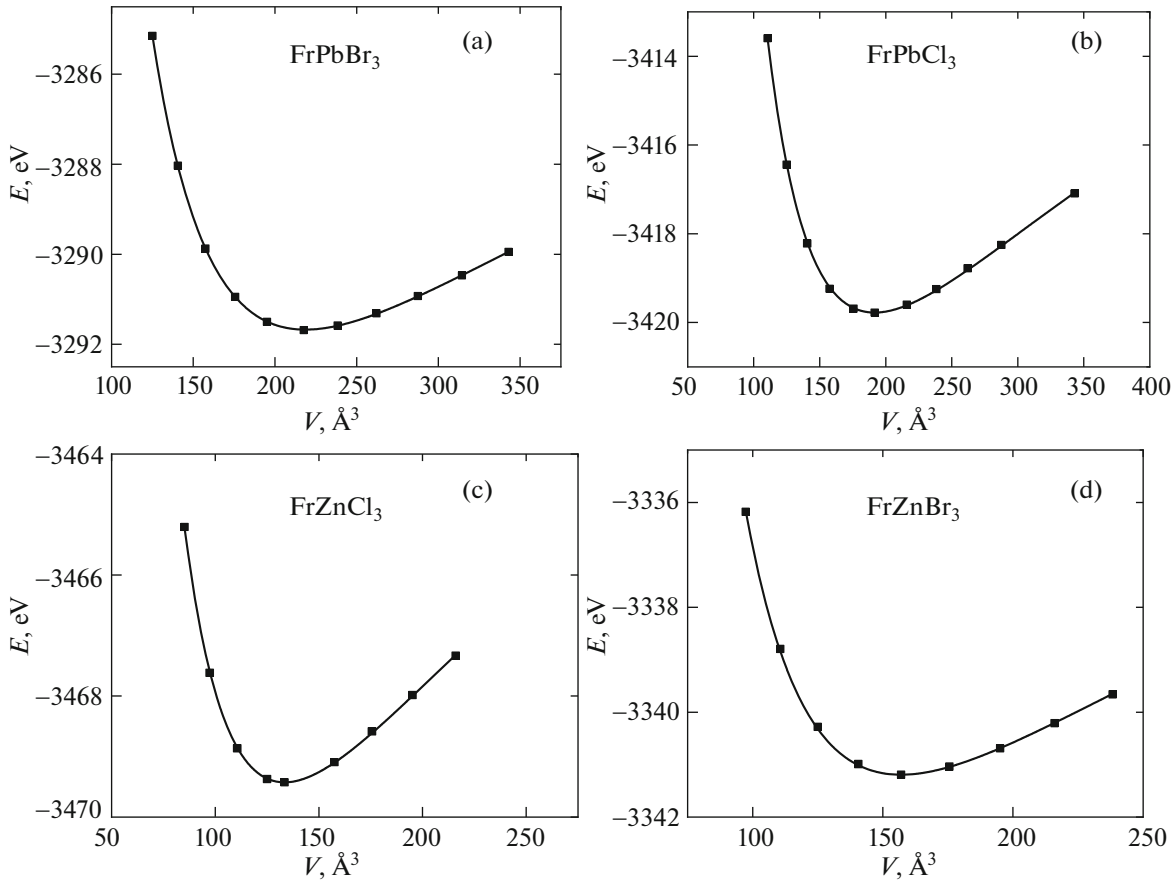

Fig. 1. Total energy vs. unit cell volume of $FrBX_3$ (B = Zn, Pb and X = Br, Cl).

firming the structural stability of the investigated compounds. Among them, $FrZnCl_3$ shows the steepest curvature, correlating with the highest bulk modulus (B_0 = 32.97 GPa), which indicates stronger bonding and greater resistance to compression. Conversely, $FrPbBr_3$ demonstrates the most gradual curve, corresponding to the lowest bulk modulus (B_0 = 18.24 GPa), and thus the highest compressibility.

Examining Table 1, the equilibrium lattice constants and volumes reveal clear trends based on the ionic sizes and bonding characteristics of the constituent elements. Compounds containing Br exhibit larger lattice constants and volumes compared to their Cl counterparts, consistent with the larger ionic radius of Br^-. Similarly, substituting Zn with Pb leads to an expansion of the lattice due to the larger ionic radius of Pb^{2+}. For instance, $FrPbBr_3$ has the largest lattice constant (a_0 = 6.015 Å) and volume (V_0 = 217.578 Å^3), while $FrZnCl_3$ shows the smallest values (a_0 = 5.111 Å, V_0 = 133.420 Å^3). These variations significantly influence the materials' electronic and optical properties.

The formation energies [26] are calculated using the equilibrium total energy $E_{\text{Total}}^{\text{FrBX}_3}$, and the equilibrium total energies per atom for bulk Fr, B (Pb or Zr) and X (Cl or Br): $E_{\text{bulk}}^{\text{Fr}}$, $E_{\text{bulk}}^{\text{Pb}}$, $E_{\text{bulk}}^{\text{Zr}}$, and $E_{\text{bulk}}^{\text{X(Cl, Br)}}$, using the following equation:

$$\Delta H_{\text{f}}\left(\text{FrBX}_3\right) = \frac{\left[E_{\text{tot(FrBX}_3)} - E_{\text{Fr}} - E_{\text{B}} - 3E_{\text{X}}\right]}{5}. \quad (1)$$

The formation energies (ΔH_{f}) across all compounds are negative, signifying thermodynamic stability and potential experimental feasibility. $FrPbCl_3$ stands out with the most negative formation energy (−3.49 eV/atom), suggesting enhanced stability relative to the other studied compounds. In contrast, $FrZnBr_3$ exhibits the least negative formation energy (−2.59 eV/atom), indicating comparatively lower stability. These findings align with the calculated cohesive energies, where stronger atomic interactions correlate with more negative values.

Furthermore, the pressure derivatives of the bulk modulus (B'), ranging between 4.47 and 5.04, suggest that the materials possess moderate anharmonicity and maintain their mechanical integrity under applied pressure. Notably, the ability to tune these properties through elemental substitution at the B-site and halo-

Table 2. Crystalline structural stability conditional parameters for cubic $FrBX_3$ (where B = Pb, Zr and X = Br, Cl) In GGA-PBE method

Alloys	Goldschmidt tolerance factor (t_G)	Octahedral factor (μ)	Ionic radii (Å)			Tolerance factor (t)	Bond length (Å)
			r_A	r_B	r_X		
$FrPbCl_3$	0.987	0.428	$Fr^+ = 1.80$ $Pb^{2+} = 0.775$ $Cl^- = 1.81$			0.99	$L_{Fr-Cl} = 4.077$ $L_{Pb-Cl} = 2.883$
$FrPbBr_3$	0.972	0.395	$Fr^+ = 1.80$ $Pb^{2+} = 0.775$ $Br^- = 1.96$			0.99	$L_{Fr-Br} = 4.253$ $L_{Pb-Br} = 3.007$
$FrZnCl_3$	1.001	0.409	$Fr^+ = 1.80$ $Zn^{2+} = 0.74$ $Cl^- = 1.81$			1	$L_{Fr-Cl} = 3.613$ $L_{Zn-Cl} = 2.555$
$FrZnBr_3$	0.985	0.378	$Fr^+ = 1.80$ $Zn^{2+} = 0.74$ $Br^- = 1.96$			1	$L_{Fr-Br} = 3.815$ $L_{Zn-Br} = 2.697$

gen positions provides flexibility for tailoring these materials to specific applications.

The structural analysis of $FrBX_3$ perovskites underscores the significant influence of B-site cation and halogen substitutions on lattice dimensions, mechanical properties, and overall stability. The tunability of these structural attributes, combined with their favorable energetic profiles, highlights the potential of these materials for various technological applications, including optoelectronic devices and radiation detectors.

3.2. Structural Stability Factors

The stability of perovskites, particularly halogenated perovskites, pertains to their ability to retain structural, chemical, and optoelectronic properties under varying environmental conditions. Stability is a key factor for these materials, especially in applications like solar cells and LEDs, where long-term performance is essential. To assess the structural stability of $FrBX_3$ (B = Zn, Pb; X = Br, Cl) perovskites, we calculated the tolerance factor (t), Goldschmidt tolerance factor (t_G), and the octahedral factor (μ) using ionic radii and bond lengths derived from optimized structural parameters (Table 2).

The tolerance factor (t) was determined based on anion–cation bond lengths in existing perovskites using the relation [27]:

$$t = \frac{L_{A-X}}{\sqrt{2}L_{B-X}}, \quad (2)$$

where L_{A-X} and L_{B-X} represent the bond lengths between the A-site cation (Fr^+) and halogen (X^-), and B-site cation (Pb^{2+} or Zn^{2+}) and halogen, respectively. Additionally, the Goldschmidt tolerance factor (t_G) and octahedral factor (μ) were calculated via the equations [28, 29]:

$$t_G = \frac{r_A + r_X}{\sqrt{2}(r_B + r_X)}, \quad (3)$$

$$\mu = \frac{r_B}{r_X}, \quad (4)$$

where r_A, r_B, and r_X are the ionic radii of Fr^+ (1.80 Å), B-site cations (Zn^{2+}: 0.74 Å, Pb^{2+}: 0.775 Å), and halogens (Cl^-: 1.81 Å, Br^-: 1.96 Å), respectively.

A perfect cubic structure is achieved when the tolerance factor equals 1. Generally, a stable perovskite structure forms when $0.8 \le t \le 1.0$; values beyond this range may lead to distorted or alternative crystal phases [30]. Table 2 reveals that all studied compounds have tolerance factors close to unity (ranging from 0.972 to 1.001), strongly supporting the formation of stable cubic perovskites. Notably, $FrZnCl_3$ and $FrZnBr_3$ exhibit tolerance factors of 1.001 and 0.985, respectively, indicating minimal structural distortions and favoring a cubic geometry. Similarly, $FrPbCl_3$ and $FrPbBr_3$ have tolerance factors of 0.987 and 0.972, respectively, also suggesting stable cubic frameworks.

The octahedral factor (μ) is crucial for determining the stability of BX_6 octahedra, with stable perovskites generally adhering to the range $0.377 < \mu < 0.895$ [31]. Lower μ-values indicate greater octahedral distortions. In this study, the μ-factors are 0.428 for

Table 3. Elastic constants, shear modulus, bulk modulus, anisotropy factor, Young's modulus, Poisson's ratio, and B_H/G_H ratio for $FrBX_3$ (B = Zn, Pb; X = Br, Cl)

Parameters	$FrZnCl_3$	$FrZnBr_3$	$FrPbCl_3$	$FrPbBr_3$
C_{11}	40.683	41.08	45.64	46.26
C_{12}	22.05	21.13	7.59	12.02
C_{44}	19.30	18.27	5.24	4.12
B	28.26	27.78	20.27078	23.43
G	14.41	14.33	9.07	7.62
B/G	1.96	1.93	2.23	3.07
E	36.94	36.68	23.68	20.62
σ	0.28	0.28	0.30	0.35
Θ_D	188.31	167.25	131.95	110.34
A	0.66	0.45	2.284	2.877

$FrPbCl_3$, 0.395 for $FrPbBr_3$, 0.409 for $FrZnCl_3$, and 0.378 for $FrZnBr_3$ (Table 2), all falling within the stability range. Among them, $FrZnBr_3$ has the lowest μ-factor, suggesting a slightly higher tendency for octahedral distortion, whereas $FrPbCl_3$ exhibits the highest μ-factor, reflecting a more rigid and stable octahedral environment.

Bond lengths further validate these observations. The Fr–X bond lengths range from 4.077 Å in $FrPbCl_3$ to 4.253 Å in $FrPbBr_3$, indicating that the substitution of Cl with the larger Br ion elongates the bond length. Similarly, B–X bond lengths vary from 2.555 Å in $FrZnCl_3$ to 3.007 Å in $FrPbBr_3$, aligning with the expected increase due to larger halogen ionic radii. These bond length variations suggest that bromide-based compounds possess slightly expanded lattices compared to their chloride counterparts, which may influence their electronic and optical properties.

The calculated stability parameters—tolerance factors, octahedral factors, and bond lengths—demonstrate that the $FrBX_3$ perovskites studied possess stable cubic structures with minimal distortions. This structural integrity, combined with favorable ionic size compatibility, positions these materials as promising candidates for optoelectronic and energy-related applications.

3.3. Elastic Aspects

Elastic properties are crucial for evaluating the mechanical behavior and practical usability of materials. Parameters such as elastic constants (C_{11}, C_{12}, C_{44}), shear modulus (G), bulk modulus (B), Young's modulus (E), Poisson's ratio (σ), and anisotropy factor (A) provide essential information on mechanical strength, flexibility, and resistance to deformation [32]. These properties are particularly vital for applications requiring mechanical stability and durability, such as flexible electronics, structural coatings, and stress-resilient components.

The mechanical stability of cubic crystals is determined by the Born stability criteria [33, 34]:

$$(C_{11} - C_{12}) > 0; \quad (C_{11} + 2C_{12}) > 0; \quad C_{11} > 0; \quad C_{44} > 0; \quad \text{and} \quad C_{12} < B < C_{11}. \tag{5}$$

As shown in Table 3, the computed elastic constants satisfy these conditions, confirming the mechanical stability of all $FrBX_3$ investigated perovskites. Among them, $FrPbBr_3$ shows the highest C_{11} value (46.26 GPa), indicating robust resistance to uniaxial compression. Conversely, $FrZnBr_3$ has the lowest C_{44} (18.27 GPa), reflecting relatively lower shear resistance.

The bulk modulus (B), indicative of resistance to uniform compression, follows the trend: $FrZnCl_3$ (28.26 GPa) > $FrZnBr_3$ (27.78 GPa) > $FrPbBr_3$ (23.43 GPa) > $FrPbCl_3$ (20.27 GPa). This order suggests that Zn-based perovskites are more incompressible compared to their Pb-based counterparts, which can be beneficial in high-pressure applications. A similar trend is observed for the shear modulus (G), underscoring the mechanical rigidity of Zn-based materials.

The B/G ratio, introduced by Pugh [35], serves as a criterion to distinguish between ductile and brittle behavior. Materials with $B/G > 1.75$ are considered ductile, while those with lower values are brittle. All examined perovskites display B/G values exceeding 1.75, confirming their ductile nature. Notably, $FrPbBr_3$ attains the highest ratio (3.07), highlighting its superior ductility, which is advantageous for applications requiring flexibility and impact absorption.

Poisson's ratio (σ), typically ranging between 0.25 and 0.35 for stable solids, provides insights into the plasticity and bonding characteristics of materials [36]. The calculated σ-values range from 0.28 to 0.35,

indicating stable and ductile structures with good plasticity. Young's modulus (E), representing the stiffness of a material, shows that Zn-based compounds, particularly $FrZnCl_3$ (36.94 GPa), possess enhanced elastic resistance relative to Pb-based variants. This indicates better dimensional stability and elastic recovery after mechanical loading, which is essential for devices that undergo repeated deformation or vibration.

The Debye temperature (Θ_D), which correlates with lattice vibrations and thermal conductivity, reveals that $FrZnCl_3$ has the highest Θ_D (188.31 K), suggesting improved thermal conduction and stability [37]. This characteristic makes Zn-based perovskites potentially more suitable for thermally demanding environments.

Elastic anisotropy, evaluated using the anisotropy factor (A), indicates the variation in mechanical properties with direction. An isotropic material has $A = 1$, while deviations from unity imply anisotropic behavior. All studied perovskites exhibit A values differing from 1, with $FrPbBr_3$ showing the most pronounced anisotropy (2.877). Such pronounced anisotropy in $FrPbBr_3$ could be exploited in direction-sensitive sensors or strain-tunable optoelectronics. In contrast, the near-isotropic behavior of $FrZnCl_3$ is favorable for uniform stress distribution, making it more robust for coating layers or encapsulation [38, 39].

Thus, elastic analysis demonstrates that $FrBX_3$ perovskites are mechanically stable, ductile, and exhibit varying degrees of anisotropy. FrZn-based perovskites, due to their higher stiffness, incompressibility and thermal stability, are ideal for structural coatings, photonic substrates, and wear-resistant optoelectronic layers. In contrast, FrPb-based perovskites, particularly $FrPbBr_3$, exhibit notable ductility and anisotropy, making them promising candidates flexible solar cells, bendable LEDs, and mechanical sensors [39–41].

The elastic anisotropy of the $FrPbBr_3$, $FrPbCl_3$, $FrZnBr_3$, and $FrZnCl_3$ compounds was analyzed through the three-dimensional (3D) and two-dimensional (2D) representations of the Young's modulus, as illustrated in Fig. 2. The 3D surface plots (Figs. 1a–1d) display the angular dependence of Young's modulus (E), highlighting the directional variation of stiffness in the studied materials.

For $FrPbBr_3$ (Fig. 1a) and $FrPbCl_3$ (Fig. 1b), the 3D plots reveal pronounced lobes along certain crystallographic directions, indicating strong elastic anisotropy. These elongated regions suggest higher stiffness along specific directions, whereas compressed areas represent softer orientations. The anisotropic behavior is attributed to the directional nature of Pb–Br and Pb–Cl bonds, consistent with previously reported anisotropy in halide perovskites [42, 43]. In contrast, $FrZnBr_3$ (Fig. 1c) and $FrZnCl_3$ (Fig. 1d) exhibit nearly cubic shapes, reflecting a near-isotropic elastic response. The smoother surfaces indicate minimal variation in stiffness with direction, which can be linked to the more ionic and less directional bonding nature of Zn–halide bonds. Notably, $FrZnCl_3$ presents slightly higher uniformity than $FrZnBr_3$, likely due to the shorter and stronger Zn–Cl bonds [43, 44].

Figures 2a–2d display the 3D surface plots of the bulk modulus (B), highlighting the resistance of the materials to uniform compression. The nearly spherical shapes observed in all four compounds indicate an overall isotropic response to hydrostatic pressure. $FrPbBr_3$ (Fig. 2a) and $FrPbCl_3$ (Fig. 2b) exhibit slight deviations from perfect sphericity, reflecting minor anisotropic compressibility along certain directions, likely due to the heavier Pb atoms and their influence on lattice vibrations [45]. $FrZnBr_3$ (Fig. 2c) and $FrZnCl_3$ (Fig. 2d) display more spherical contours, underscoring their uniform compressive resistance. Among the studied materials, $FrZnCl_3$ demonstrates the highest isotropy in bulk modulus distribution, which can be attributed to the enhanced bonding strength of Zn–Cl interactions [45].

The shear modulus (G) surfaces, shown in Figs. 3a–3d, provide further understanding of the resistance to shape deformation. $FrPbBr_3$ and $FrPbCl_3$ exhibit noticeable anisotropy, with lobes and indentations indicating varying shear stiffness along different crystallographic axes. Such anisotropic behavior is primarily due to the directional bonding and lattice distortions influenced by the Pb–halide interactions [42]. Conversely, $FrZnBr_3$ and $FrZnCl_3$ present relatively smoother surfaces, signifying reduced anisotropy. The smoother shear modulus profile of $FrZnCl_3$ further confirms its higher structural stability and isotropic mechanical response, reinforcing the effect of Cl's smaller ionic radius and stronger bonding compared to Br [44, 45].

Further insight into the elastic anisotropy is provided by the 2D transverse sections (Figs. 2e–2h), taken in the (X–Y), (X–Z), and (Y–Z) planes. For $FrPbBr_3$ (Fig. 2e) and $FrPbCl_3$ (Fig. 1f), the plots exhibit four-lobed patterns, emphasizing significant anisotropy in the (X–Y) plane. The outermost curves correspond to directions with higher Young's modulus, while the innermost curves indicate softer mechanical responses. These anisotropic features stem from the layered atomic arrangement and variable bond strengths along different crystallographic axes [45]. Conversely, the 2D plots for $FrZnBr_3$ (Fig. 2g) and $FrZnCl_3$ (Fig. 2h) show nearly circular contours, confirming their near-isotropic behavior. Among them, $FrZnCl_3$ displays the most uniform distribution, consistent with its higher structural symmetry and the presence of smaller Cl ions. The slight inward curvature observed in $FrZnBr_3$ suggests weak anisotropy influenced by the larger Br ions [45].

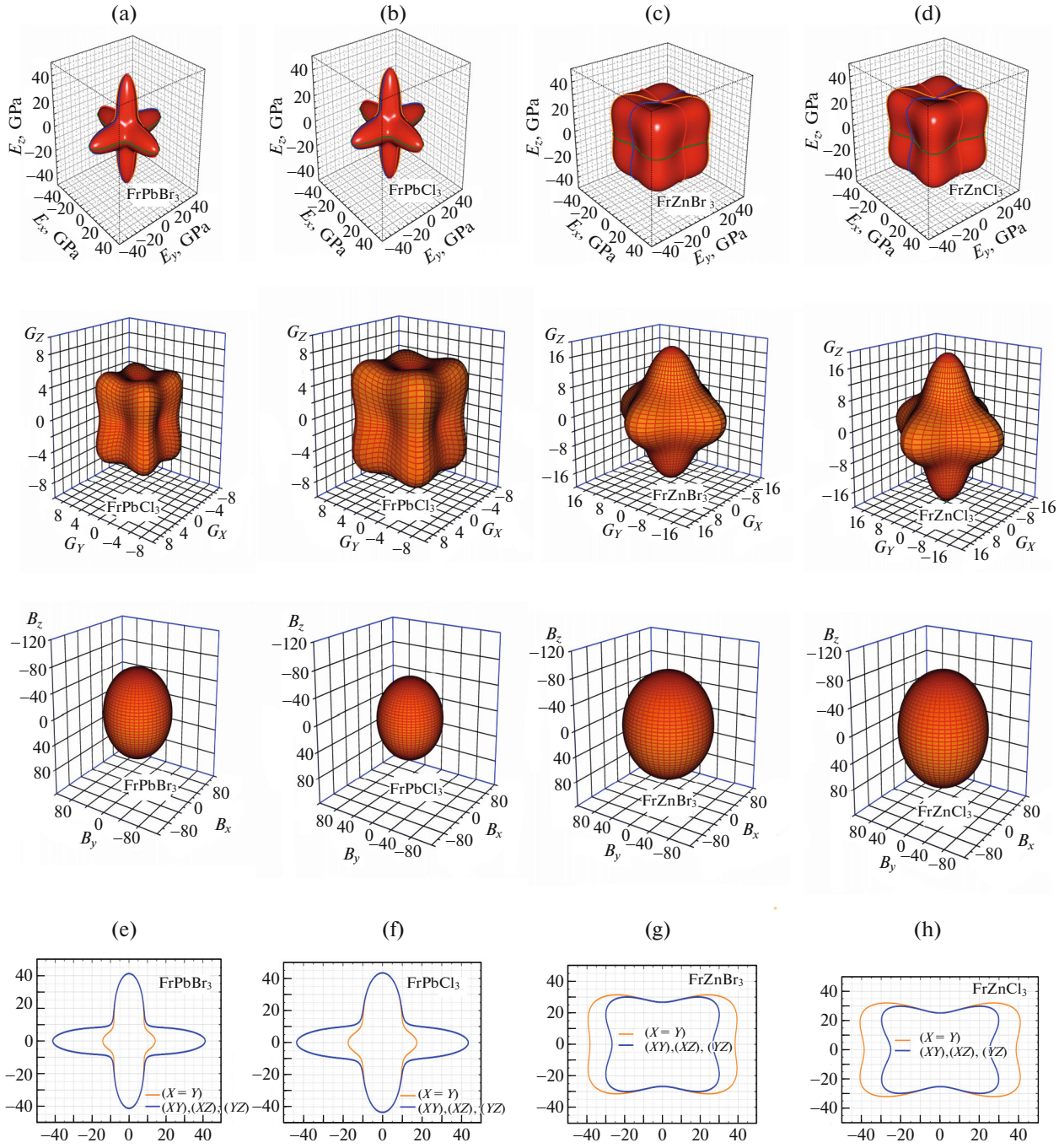

Fig. 2. Graphs of the 3D surface of the Young's modulus, bulk modulus and Shear moduli (a) $FrPbBr_3$, (b) $FrPbCl_3$, (c) $FrZnBr_3$, and (d) $FrZnCl_3$, (e, f, g, and h) the transverse sections of the Young's modulus in separated planes, respectively.

The differences in elastic anisotropy between FrPb- and FrZn-based compounds have significant technological implications. The pronounced anisotropy in $FrPbBr_3$ and $FrPbCl_3$ may benefit applications requiring directional mechanical reinforcement, such as flexible electronics where stress distribution varies with orientation. In contrast, the near-isotropic mechanical behavior of $FrZnBr_3$ and $FrZnCl_3$ makes them suitable for coatings and substrates in optoelectronic devices, where uniform mechanical properties are crucial [42–46]. Additionally, the higher isotropy observed in $FrZnCl_3$ suggests its potential advantage in devices exposed to multidirectional mechanical stresses [42–46].

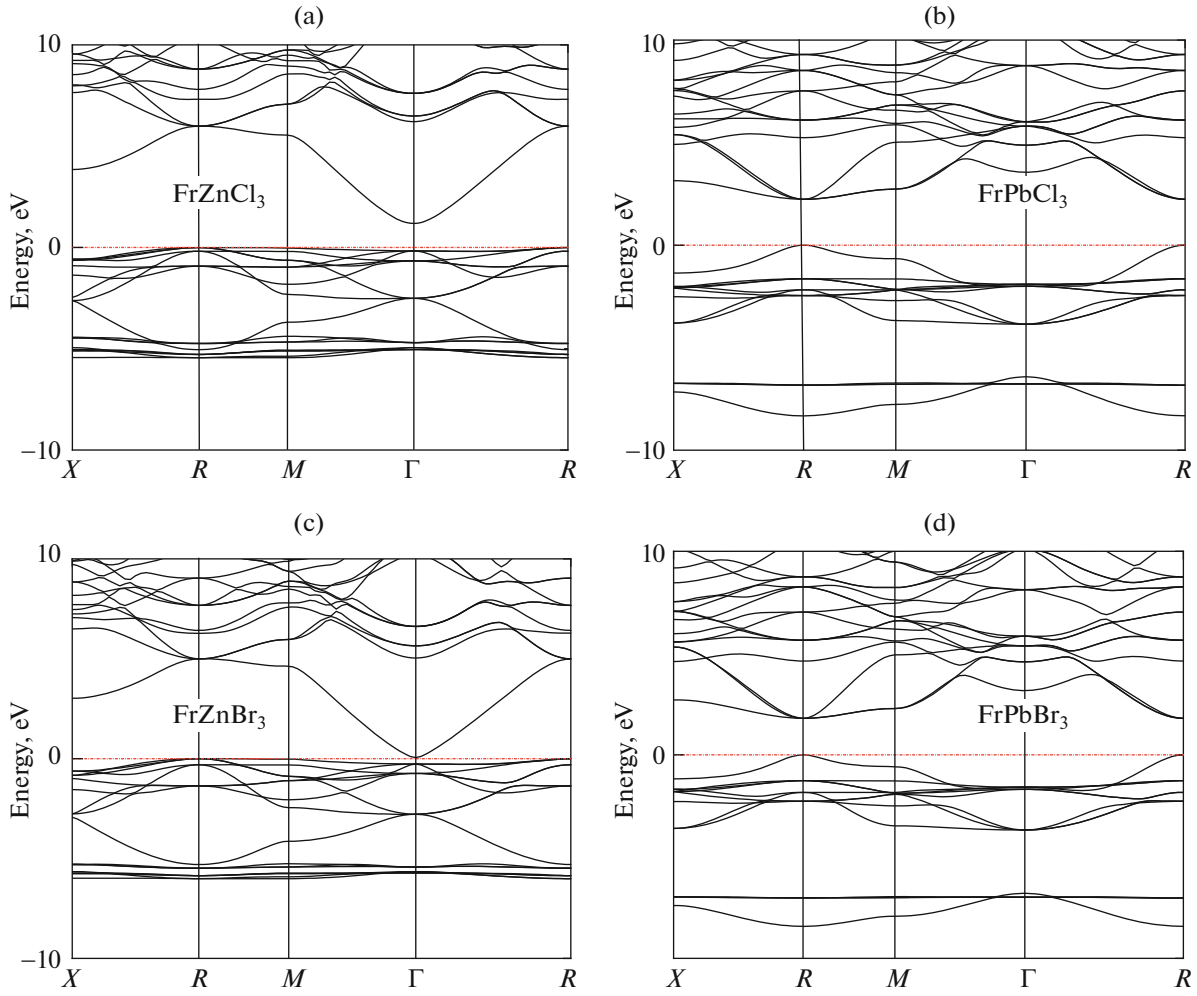

Fig. 3. Spin polarized band structure of $FrBX_3$ (B = Zn, Pb and X = Br, Cl) at their equilibrium lattice.

3.4. Electronic Aspects

Analyzing the electronic band structure is vital for understanding the relationship between the physical properties of crystalline solids and their atomic arrangement. This analysis provides essential information on charge carrier dynamics, electrical resistivity, and optical responses, which are critical for applications in electronics and optoelectronics. By examining how electron energy varies with momentum in the reciprocal lattice, one can assess the suitability of materials for devices like solar cells, photodetectors, and transistors.

To explore the electronic characteristics of cubic $FrBX_3$ (B = Pb, Zn; X = Cl, Br) perovskites, we employed the generalized gradient approximation with the Perdew–Burke–Ernzerhof (GGA-PBE) functional to calculate their band structures along the high-symmetry *k*-path *R*–Γ–*X*–*M*–Γ (Fig. 3). The computed band gaps, listed in Table 4, reveal that all studied compounds exhibit semiconducting behavior, with the Fermi level set at 0 eV. For $FrPbCl_3$ and $FrPbBr_3$, both the valence band maximum (VBM) and conduction band minimum (CBM) occur at the *R* point, indicating a direct band gap. Conversely, $FrZnCl_3$ and $FrZnBr_3$ display an indirect band gap, with the VBM at *R* and the CBM at Γ. At zero pressure, the calculated band gap values are 2.237 eV for $FrPbCl_3$, 1.795 eV for $FrPbBr_3$, 1.185 eV for $FrZnCl_3$, and 0.057 eV for $FrZnBr_3$.

A noticeable trend emerges when substituting Zn with Pb at the B-site: the band gap decreases for the same halogen atom, suggesting enhanced electronic delocalization due to Pb's larger atomic orbitals. Similarly, replacing Cl with Br at the X-site reduces the band gap, a consequence of the increased atomic size and decreased electronegativity of bromine, which leads to higher valence band energies (Fig. 3). Such tunability of the band gap through elemental substitution is advantageous for tailoring the optical absorption properties of these materials for specific applications.

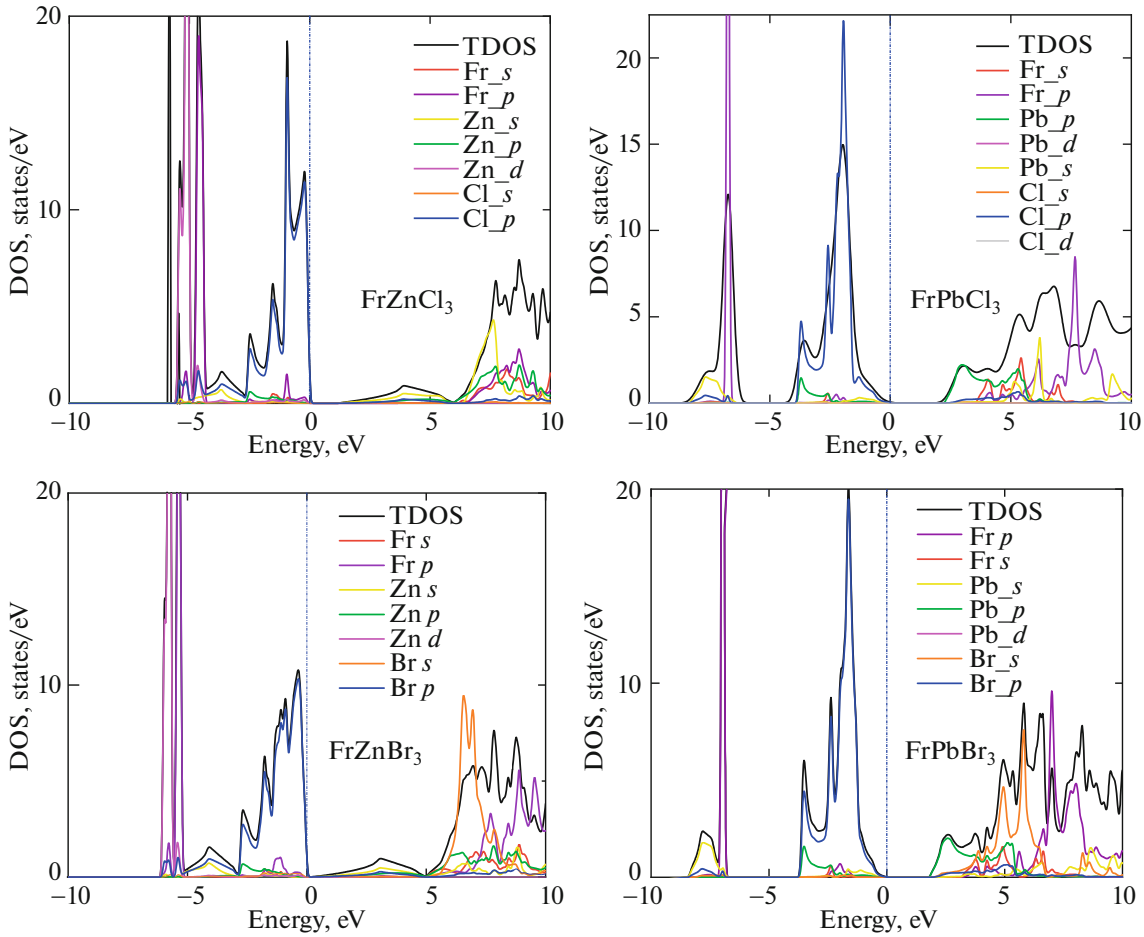

Fig. 4. The total and partial density of states of the $FrBX_3$ (B = Zn, Pb and X = Br, Cl) calculated by GGA.

The total density of states (TDOS) and partial density of states (PDOS) for $FrBX_3$ perovskites are depicted in Fig. 4, covering an energy range from −10 to 10 eV. The valence band, spanning from −10 to 0 eV, primarily arises from the halogen (Cl and Br) *p*-states, whereas the conduction band (0–10 eV) exhibits significant contributions from the B-site cations. In $FrPbCl_3$ and $FrPbBr_3$, Pb-*p* orbitals dominate the conduction band region up to approximately 5 eV, indicating strong hybridization with halogen *p*-states. This hybridization implies a covalent character in Pb–halide bonds. In contrast, $FrZnCl_3$ and $FrZnBr_3$ show notable contributions from Zn-*s* and Zn-*p* states in the conduction band, coupled with halogen *p*-states. The stronger hybridization between Zn and Cl compared to Zn and Br correlates with the observed differences in band gap and mechanical stability.

The PDOS analysis reveals that halogen atoms contribute most significantly near the Fermi level, reflecting their pivotal role in determining the valence band structure. While the Fr atom exhibits minimal electronic participation, its presence influences the lattice constants and overall stability. Notably, the proximity of the Fermi level to the valence band maximum in all compounds suggests an *n*-type semiconducting behavior, favorable for electron transport applications. The ability to manipulate electronic properties through compositional variation enhances the potential of $FrBX_3$ perovskites in photovoltaic and optoelectronic devices.

3.5. Optical Aspects

The complex dielectric function, $(\varepsilon_1 + i\varepsilon_2)$, plays a critical role in understanding a material's interaction with electromagnetic radiation. The real part (ε_1) represents dispersion and polarization, while the imaginary part (ε_2) accounts for optical absorption [47].

Figure 5a illustrates the real and imaginary parts of the dielectric functions for $FrPbBr_3$ and $FrPbCl_3$. The static dielectric constants $(\varepsilon_1(0))$ for both compounds are around 5–6, indicating moderate polarizability. Notably, the imaginary part (ε_2) exhibits significant absorption peaks in the energy range of 2–10 eV. $FrPbBr_3$ shows slightly higher absorption in the lower

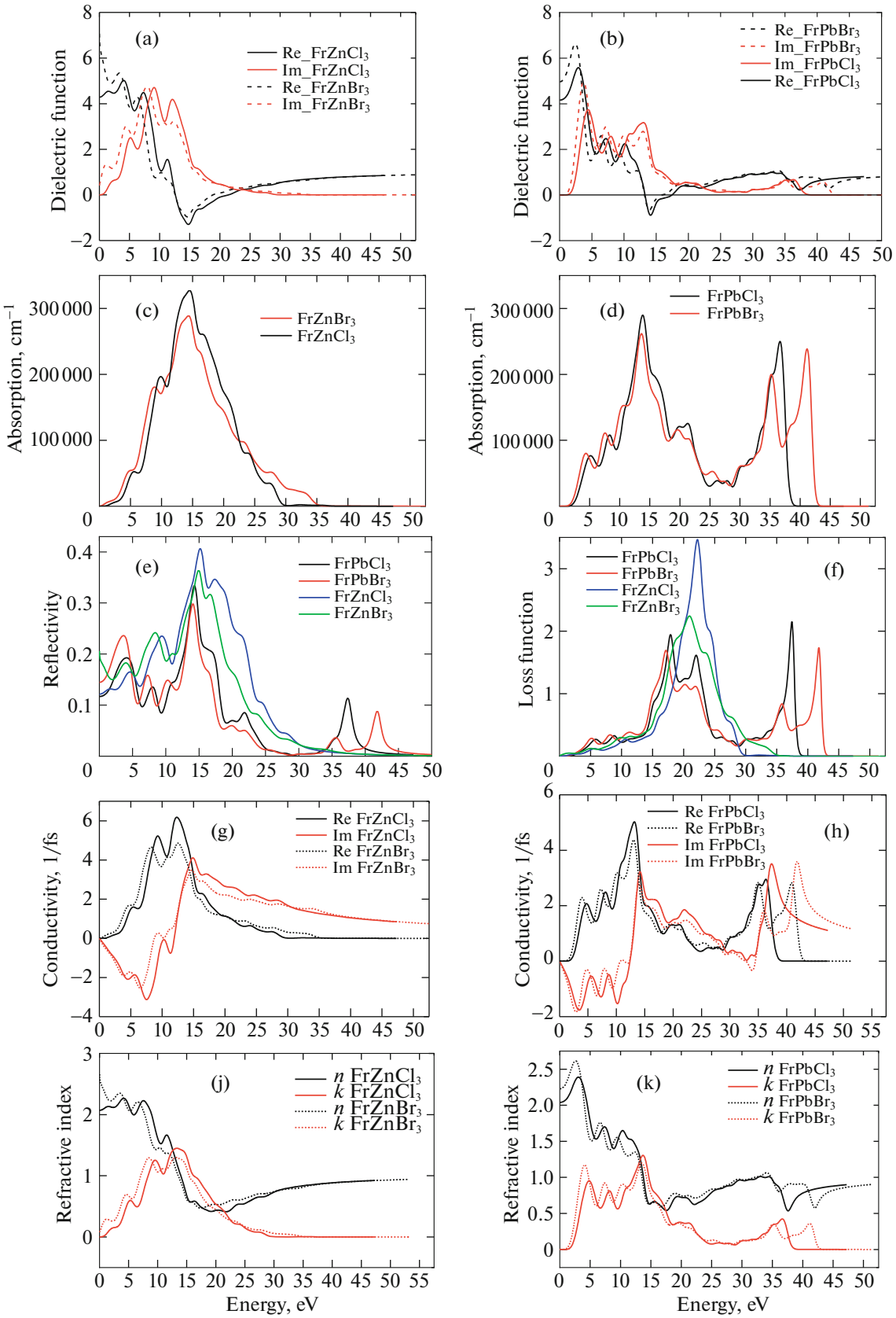

Fig. 5. (a, b) Dielectric function analysis, (c, d) absorption coefficient analysis, (e, f) reflectivity and energy loss function analysis, (g, h) optical conductivity analysis, (j, k) refractive index analysis.

energy region, suggesting stronger absorption in the visible to ultraviolet (UV) range. The real part (ε_1) experiences a sharp rise near the absorption edge (~2 eV) before decreasing beyond 10 eV. Negative values of (ε_1) between 12–20 eV indicate plasma resonance, implying high reflectivity in this region [47]. This behavior suggests that $FrPbBr_3$ is more suitable for optoelectronic applications requiring visible light absorption compared to $FrPbCl_3$.

Figure 5b presents the dielectric function components for $FrZnCl_3$ and $FrZnBr_3$. Both compounds have static dielectric constants near 5, similar to those observed in FrPb-based materials, signifying comparable polarizability. The imaginary part (ε_2) shows prominent absorption peaks within 3–12 eV. $FrZnBr_3$ displays higher intensity in the visible range, supporting its use in photovoltaic and photodetector applications. The real part (ε_1) shows strong dispersion below 10 eV and displays negative values between 15–25 eV, reflecting metallic characteristics and high reflectivity in the UV region [47]. These properties highlight $FrZnBr_3$'s potential for broad-spectrum photon absorption.

Comparing both sets of compounds reveals that bromide-based materials $FrPbBr_3$ and $FrZnBr_3$ consistently exhibit higher absorption in the visible spectrum than their chloride counterparts. This characteristic makes them favorable for solar energy and optoelectronic device applications [46]. The negative regions of (ε_1) in all materials indicate metallic-like reflectivity at high photon energies, suggesting their utility in UV-protective coatings. Additionally, the moderate static dielectric constants across the compounds point to their potential in semiconductor applications, where balanced polarization and screening effects are essential.

These findings align with previous studies highlighting the importance of dielectric properties in optimizing materials for optoelectronic applications [46]. Further investigations of refractive index and reflectivity, derived from the presented dielectric functions, would provide deeper insights into their practical applications.

In Fig. 5c, the absorption spectra of $FrPbCl_3$ and $FrPbBr_3$ reveal prominent absorption peaks between approximately 5–20, 25–35, and 35–45 eV. $FrPbCl_3$ exhibits higher absorption intensities in the high-energy region (above 35 eV), indicating stronger interband transitions in comparison to $FrPbBr_3$. These peaks are attributed to electronic transitions from the valence to conduction bands, with variations due to the differing atomic masses and electronegativity of Cl and Br atoms. The shift of $FrPbBr_3$ peaks to lower energies suggests that Br incorporation reduces the band gap, allowing for earlier photon absorption.

Figure 5d compares the absorption spectra of $FrZnCl_3$ and $FrZnBr_3$. Both compounds demonstrate intense absorption in the 5–20 eV range, with $FrZnCl_3$ showing slightly higher absorption peaks. The main absorption peak occurs around 15 eV for both materials, indicating strong photon absorption within the ultraviolet region. Beyond 30 eV, the absorption coefficient rapidly decreases for both compounds, suggesting limited absorption capabilities in the high-energy spectrum. The marginal shift of the $FrZnBr_3$ peaks toward lower energies emphasizes halogen substitution effects on the optical properties, making Br-containing compounds more suitable for applications requiring lower-energy photon absorption.

Figure 5e illustrates the reflectivity spectra of the studied compounds. All materials exhibit high reflectivity in the UV region with noticeable peaks between 10–20 eV. $FrZnCl_3$ and $FrZnBr_3$ show relatively higher reflectivity compared to their lead-based counterparts, with maximum reflectivity values around 0.4 for $FrZnCl_3$. The elevated reflectivity in the UV region suggests these compounds could be effective coatings for UV-reflective devices. Beyond 20 eV, reflectivity gradually decreases for all materials, indicating reduced reflection efficiency at higher energies.

Figure 6f shows the energy loss function (ELF), which characterizes the energy loss of fast electrons traversing the materials, revealing plasmonic resonance features. All compounds exhibit pronounced peaks between 20–25 eV, with $FrZnCl_3$ showing the highest peak intensity, indicating a strong plasmonic response. The observed peaks correspond to the plasma frequency where the material exhibits maximum energy loss, crucial for applications in electron energy loss spectroscopy and plasmonic devices. Additional smaller peaks are observed beyond 30 eV, especially for $FrPbCl_3$ and $FrPbBr_3$, indicating secondary plasmonic resonances influenced by the heavier Pb atoms.

Overall, these perovskites demonstrate notable UV absorption, moderate reflectivity, and distinct plasmonic features. The influence of halogen substitution is evident in the shift of absorption peaks and reflectivity behavior, offering pathways to tailor the optical properties for specific optoelectronic and photovoltaic applications.

Figures 5g and 5h present the real and imaginary parts of optical conductivity for the $FrPbCl_3$, $FrPbBr_3$, $FrZnCl_3$, and $FrZnBr_3$ compounds as functions of photon energy. These plots provide crucial insights into the electronic transitions and charge carrier dynamics within the studied materials.

In Fig. 5g, which illustrates $FrPbCl_3$ and $FrPbBr_3$, the real part of the conductivity (Re) exhibits distinct peaks around 12–15 and 35–40 eV, indicating strong interband electronic transitions. $FrPbCl_3$ shows higher conductivity peaks compared to $FrPbBr_3$, suggesting better carrier transport and a higher density of states near the conduction band. The imaginary part (Im),

representing the energy dissipation within the material, follows similar trends with prominent peaks at corresponding energies, reflecting high absorption in those regions.

Figure 5h shows the optical conductivity for $FrZnCl_3$ and $FrZnBr_3$. Both compounds display notable conductivity peaks between 10–20 eV, with $FrZnCl_3$ having slightly higher real conductivity values. The imaginary part follows a decreasing trend beyond 20 eV, indicating reduced energy absorption at higher photon energies. These conductivity profiles are consistent with the absorption and reflectivity behaviors discussed earlier, reaffirming the materials' potential for optoelectronic applications.

The differences observed between the chloride and bromide counterparts can be attributed to variations in their electronic band structures and bonding environments. Notably, the shift of peaks to lower energies in bromide-based compounds reflects their narrower band gaps, enhancing their absorption in the visible range. These findings underscore the impact of halogen substitution on the electronic and optical properties of the materials, offering a tunable approach for designing devices with tailored optical responses.

Figures 5j and 5k depict the refractive index (n) and extinction coefficient (k) of $FrPbCl_3$, $FrPbBr_3$, $FrZnCl_3$, and $FrZnBr_3$ as functions of photon energy. In Fig. 5j, FrPb-based compounds exhibit maximum static refractive indices at approximately 2.5 ($FrPbCl_3$) and 2.3 ($FrPbBr_3$), indicating strong light-matter interaction at low photon energies. Both compounds display a decreasing trend with increasing photon energy, suggesting reduced optical density at higher energies. The extinction coefficient shows prominent peaks around 12 and 35 eV, corresponding to strong absorption regions.

Figure 5k shows the refractive index and extinction coefficient for FrZn-based materials. $FrZnCl_3$ exhibits a higher static refractive index (~2.6) than $FrZnBr_3$ (~2.4), indicating stronger initial optical interaction. Both compounds show decreasing n values beyond 10 eV, with $FrZnBr_3$ declining more rapidly. The extinction coefficient peaks near 11–13 and 30 eV indicate the energy regions where absorption is most pronounced.

The analysis reveals that FrZn-based compounds exhibit higher refractive indices and extinction coefficients at lower energies compared to FrPb-based compounds, suggesting superior optical absorption and light-guiding capabilities. These properties make them potential candidates for applications in photonic and optoelectronic devices, including solar cells and optical sensors.

4. CONCLUSIONS

This comprehensive investigation provides valuable insights into the structural, electronic, optical, and elastic properties of inorganic metal halide perovskites $FrBX_3$ (B = Pb, Zr; X = Br, Cl) through first-principles calculations based on density functional theory (DFT). The structural analysis, validated by optimized lattice parameters and negative formation energies, confirms the thermodynamic stability of all investigated compounds, ensuring their feasibility for practical applications. The electronic band structure reveals that $FrZnX_3$ compounds possess direct band gaps, whereas $FrPbX_3$ compounds exhibit indirect band gaps. The observed decreasing trend in band gaps—from $FrPbCl_3$ to $FrZnBr_3$—highlights the tunability of these materials for optoelectronic applications. Notably, the extremely narrow band gap of $FrZnBr_3$ suggests potential use in infrared detection and thermophotovoltaic devices, while the moderate band gaps of $FrPbCl_3$ and $FrPbBr_3$ make them suitable for visible-light-driven photovoltaic applications.

The optical analysis reveals strong absorption in the visible region, high dielectric constants, and favorable refractive indices, indicating the ability of these materials to efficiently harvest solar energy with minimal optical losses. Such properties not only enhance light absorption but also improve charge carrier generation, essential for high-efficiency solar cells. Moreover, the calculated optical parameters suggest potential applicability in photodetectors, light-emitting diodes (LEDs), and other optoelectronic devices beyond solar cells.

From a mechanical perspective, the calculated elastic constants, bulk modulus, shear modulus, and Poisson's ratio confirm that all studied compounds meet the Born stability criteria, ensuring mechanical robustness. The observed ductility, indicated by the positive values of Poisson's ratio and favorable Pugh's ratio, suggests that these materials can endure mechanical stress without fracturing, which is crucial for long-term device reliability. Furthermore, the moderate elastic anisotropy offers an advantageous balance between mechanical stability and flexibility, facilitating the development of thin-film devices that can withstand fabrication processes and operational stresses without compromising performance.

The synergy between structural stability, tunable electronic band gaps, exceptional optical absorption, and mechanical resilience positions the Fr-based perovskites as promising candidates for next-generation photovoltaic devices, optoelectronic components, and flexible electronics. To fully realize their potential, future research should focus on experimental validation, investigating the effects of doping, defect engineering, and long-term environmental stability. Additionally, exploring heterostructures and interfacial behavior with other materials could pave the way for

the development of multi-functional, high-performance optoelectronic devices.

ACKNOWLEDGMENTS

The authors (I. Bensehil, T. Ghellab, Z. Charifi, and H. Baaziz) would like to thank the general directorate for scientific research and technological development for their financial support during the realization of this work.

FUNDING

This work was supported by ongoing institutional funding. No additional grants to carry out or direct this particular research were obtained.

CONFLICT OF INTEREST

The authors of this work declare that they have no conflicts of interest.

REFERENCES

1. Q. A. Akkerman and L. Manna, ACS Energy Lett. **5** (2), 604 (2020).
2. H. Kim, M. Gil, and H. Kang, Electronics **13**, 3572 (2024).
3. Q. Chen, N. De Marco, Y. Yang, et al., Nano Today **10**, 355 (2015).
4. H. Kim, et al., Small Methods **2** (3), 1700310 (2018).
5. T. Tang and Y. Tang, Mater. Today Commun. **34**, 105431 (2023).
6. P. Cheng, K. Han, and J. Chen, ACS Mater. Lett. **5**, 60 (2023).
7. S. D. Stranks and H. J. Snaith, Nat. Nanotechnol. **10**, 391 (2015).
8. H. Park, C. Ha, and J.-H. Lee, J. Mater. Chem. A **8**, 24353(2020).
9. S. Shahrokhi, W. Gao, Y. Yang, et al., Small Methods **4**, 2000149 (2020).
10. N. Hasan, M. Arifuzzaman, and A. Kabir, RSC Adv. **12**, 7961 (2022).
11. S. W. Eaton, M. Lai, N. A. Gibson, et al., Proc. Natl. Acad. Sci. U. S. A. **113**, 1993 (2016).
12. B. Jeong, L. Veith, T. J. A. M. Smolders, et al., Adv. Mater. **33**, 2100486 (2021).
13. G. I. Choi and H. W. Choi, Nanomaterials **12**, 1132 (2022).
14. Z. Liu, W. Qiu, X. Peng, et al., Adv. Mater. **33**, 2103268 (2021).
15. M. Wuttig, C.-F. Schön, M. Schumacher, et al., Adv. Funct. Mater. **32**, 2110166 (2022).
16. P. Pitriana, T. D. K. Wungu, H, Herman, et al., J. Phys. Conf. Ser. **1204**, 012107 (2019).
17. U. Bushra, A. Rahman, M. T. Ahmed, et al., Phys. B: Condens. Matter **697**, 41670 (2025).
18. S. J. Clark, M. D. Segall, C. J. Pickard, et al., Cryst. Mater. **4**, 220 (2005).
19. D. Vanderbilt, Phys. Rev. **41**, 7892 (1990).
20. V. Milman and M. C. Warren, J. Phys. Condens. Matter. **13**, 241 (2001).
21. W. Voigt, *Lehrbuch der Kristallphysik* (Teubner, Leipzig, 1928.
22. A. Reuß, Angew. Math. Mech. **9**, 49 (1929).
23. R. Hill, Proc. Phys. Soc. A **65**, 349 (1952).
24. M. K. Hussain, B. J, Kahdum, R. Paudel, et al., Electron. Mater. **52**, 258 (2023).
25. F. D. Murnaghan, Proc. Natl. Acad. Sci. U. S. A. **30**, 244 (1944).
26. M. M. Hasan, Heliyon **10**, e34824 (2024).
27. R. Y. Alyoubi, Phys. Lett. A **35**, 2150056 (2021).
28. V. M. Goldschmidt, Naturwissenschaften **14**, 477 (1926).
29. J. D. Feng, Vacuum **164**, 186 (2019).
30. R. Kour, S. Arya, S. Verma, et al., Global Challenges **3**, 190005 (2019).
31. Q. Sun and W. J. Yin, J. Am. Chem. Soc. **139**, 14905 (2017).
32. J. Smith and T. Lee, J. Mater. Sci. **57** (14), 4625 (2022).
33. M. Born and K. Huang, *Dynamical Theory of Crystal Lattices* (Oxford University Press, 1954).
34. S. Al Selgin, N. N. Cavdar, and N. Arikan, J. Energy Storage **80**, 110402 (2024).
35. S. F. Pugh, Philos. Mag. **45**, 823 (1954).
36. S. D. Poisson, Mem. Acad. Sci. Paris **8**, 357 (1829).
37. O. L. Anderson, J. Phys. Chem. Solids **24**, 909 (1963).
38. S. I. Ranganathan and M. Ostoja-Starzewski, Phys. Rev. Lett. **101**, 055504 (2008).
39. N. Arikan, S. Al Selgin, and A. Iyigor, J. Mol. Modell. **28**, 366 (2022).
40. Y. Zhang and L. Wang, Comput. Mater. Sci. **193**, 110387 (2021).
41. X. Q. Chen, H. Niu, D. Li, et al., Intermetallics **19**, 1275 (2011).
42. Q. Li, L. Zhang, Z. Chen, et al., J. Mater. Chem. A **7**, 16089 (2019).
43. G. Liu, L. Kong, W. Yang, et al., Mater. Today **27**, 91 (2019).
44. Y. Shi, Y. Zhou, Z. Ma, G. Xiao, K. Wang, and B. Zou, et al., J. Mater. Chem. C **8**, 12755 (2020).
45. H. Lee, D. Ko, and C. Lee, ACS Appl. Mater. Interfaces **11** (12), 11667 (2019).
46. M. B. Mansur, F. Farhan, N. J. Nisha, et al., J. Inorg. Organomet. Polym. Mater. (2025).
47. A. J. Freeman and J. E. Jaffe, Phys. Rev. **45**, 8163 (1992).